

Multistep nucleation of nanocrystals in aqueous solution

N. Duane Loh^{1,2}, Soumyo Sen³, Michel Bosman^{4,5}, Shu Fen Tan⁶, Jun Zhong^{1,2}, Christian A. Nijhuis^{6,7*}, Petr Král^{3,8*}, Paul Matsudaira^{2,9} and Utkur Mirsaidov^{1,2,7,10*}

The nucleation and growth of solids from solutions impacts many natural processes and is fundamental to applications in materials engineering and medicine. For a crystalline solid, the nucleus is a nanoscale cluster of ordered atoms that forms through mechanisms still poorly understood. In particular, it is unclear whether a nucleus forms spontaneously from solution via a single- or multiple-step process. Here, using *in situ* electron microscopy, we show how gold and silver nanocrystals nucleate from supersaturated aqueous solutions in three distinct steps: spinodal decomposition into solute-rich and solute-poor liquid phases, nucleation of amorphous nanoclusters within the metal-rich liquid phase, followed by crystallization of these amorphous clusters. Our *ab initio* calculations on gold nucleation suggest that these steps might be associated with strong gold-gold atom coupling and water-mediated metastable gold complexes. The understanding of intermediate steps in nuclei formation has important implications for the formation and growth of both crystalline and amorphous materials.

Nucleation is commonly described by the classical nucleation theory (CNT) in which a nascent phase, termed ‘nucleus’, emerges from solution in a single step^{1–5}. Although CNT successfully describes various phenomena, such as the condensation of water droplets from vapour⁶, it fails for more-complex systems. For example, CNT predicts homogeneous nucleation rates for lysozyme⁷ and ice⁸ that are at least ten orders of magnitude slower than experimentally measured rates. To account for the large discrepancies in the crystallization rates^{1,7,9}, most non-classical nucleation models introduce an additional step that precedes nucleation^{3,9,10}. One such mechanism involves a spinodal decomposition¹¹ of two-component solutions to form solute-rich and solute-poor liquid phases followed by the formation of nuclei in the solute-rich liquid phase. This multistep mechanism has been proposed for the nucleation of CaCO₃ in water^{12,13}, lysosome crystals in water³ and others¹⁴. To develop models for nucleation that deviate from CNT, direct experimental probing of the nanoscale dynamics of alternative nucleation pathways is necessary.

Although others have studied post-nucleation crystal growth at the nanometre scale^{15–17} using recent advances in *in situ* transmission electron microscopy (TEM)^{15,18}, here we extend this TEM method to observe directly each step in the nucleation pathway of gold nanoparticles in water. We chose to investigate the nucleation pathway of gold and silver from water because previous studies of gold crystallization predicted that a dense liquid phase should nucleate from a supersaturated solution^{19,20} (Supplementary Section 11A), and that nanocrystals form rapidly from this dense phase^{21,22} (Supplementary Section 11B), probably via spinodal decomposition²⁰ (Supplementary Section 12). These studies,

however, did not uncover the dynamics of the phases preceding nucleation. To test these predictions, we used *in situ* TEM to follow the dynamics of gold nucleating in a 30 nm thick aqueous solution (Methods).

Results and discussions

Real-time imaging (Fig. 1a) shows two intermediate states of gold nucleation. Between the initial homogeneous solution of gold (left panel) and the final crystalline solid nanoparticle (right panel) two sequential states (middle panels) appear: a two-phase aqueous mixture and a non-crystalline cluster. The initial phase separation can be explained by the well-documented fact that high-energy electrons²³ generate solvated electrons in the aqueous gold solution, which leads to a rapid reduction of Au³⁺ ions to Au⁰ (ref. 23) (Supplementary Sections 2 and 4). Other short-lived species created during the radiolysis of water do not promote gold nucleation owing to their lower redox potentials (Supplementary Section 4). Qualitative molecular dynamics simulations (Fig. 1b and Supplementary Section 14) confirm that gold nanocrystals nucleate from the supersaturated aqueous solution of Au⁰ in three steps: (1) the solution demixes into gold-poor and gold-rich aqueous phases by spinodal decomposition, (2) amorphous gold nanoclusters arise from the gold-rich phase and (3) the amorphous nanoclusters crystallize. These three steps are not specific for gold nucleation, but also appear when silver nanocrystals form in water (Fig. 1c and Supplementary Section 15), which implies that multistep nucleation probably applies to other noble-metal nanoclusters, an important class of catalysts. We present our quantitative analysis methods below, focusing on gold as an example.

¹Department of Physics, National University of Singapore, 2 Science Drive 3, Singapore 117551. ²Centre for Bioimaging Sciences, Department of Biological Sciences, National University of Singapore, 14 Science Drive 4, Singapore 117543. ³Department of Chemistry, University of Illinois at Chicago, Chicago, Illinois 60607, USA. ⁴Institute of Materials Research and Engineering, A*STAR (Agency for Science, Technology and Research), 2 Fusionopolis Way, Singapore 138634. ⁵Department of Materials Science and Engineering, National University of Singapore, 9 Engineering Drive 1, Singapore 117575. ⁶Department of Chemistry, National University of Singapore, 3 Science Drive 3, Singapore 117543. ⁷Centre for Advanced 2D Materials and Graphene Research Centre, National University of Singapore, 6 Science Drive 2, Singapore 117546. ⁸Department of Physics and Biopharmaceutical Sciences, University of Illinois at Chicago, Chicago, Illinois 60607, USA. ⁹MechanoBiology Institute, National University of Singapore, 5A Engineering Drive 1, Singapore 117576. ¹⁰NanoCore, National University of Singapore, 4 Engineering Drive 3, Singapore 117576. *e-mail: christian.nijhuis@nus.edu.sg; pkral@uic.edu; mirsaidov@nus.edu.sg

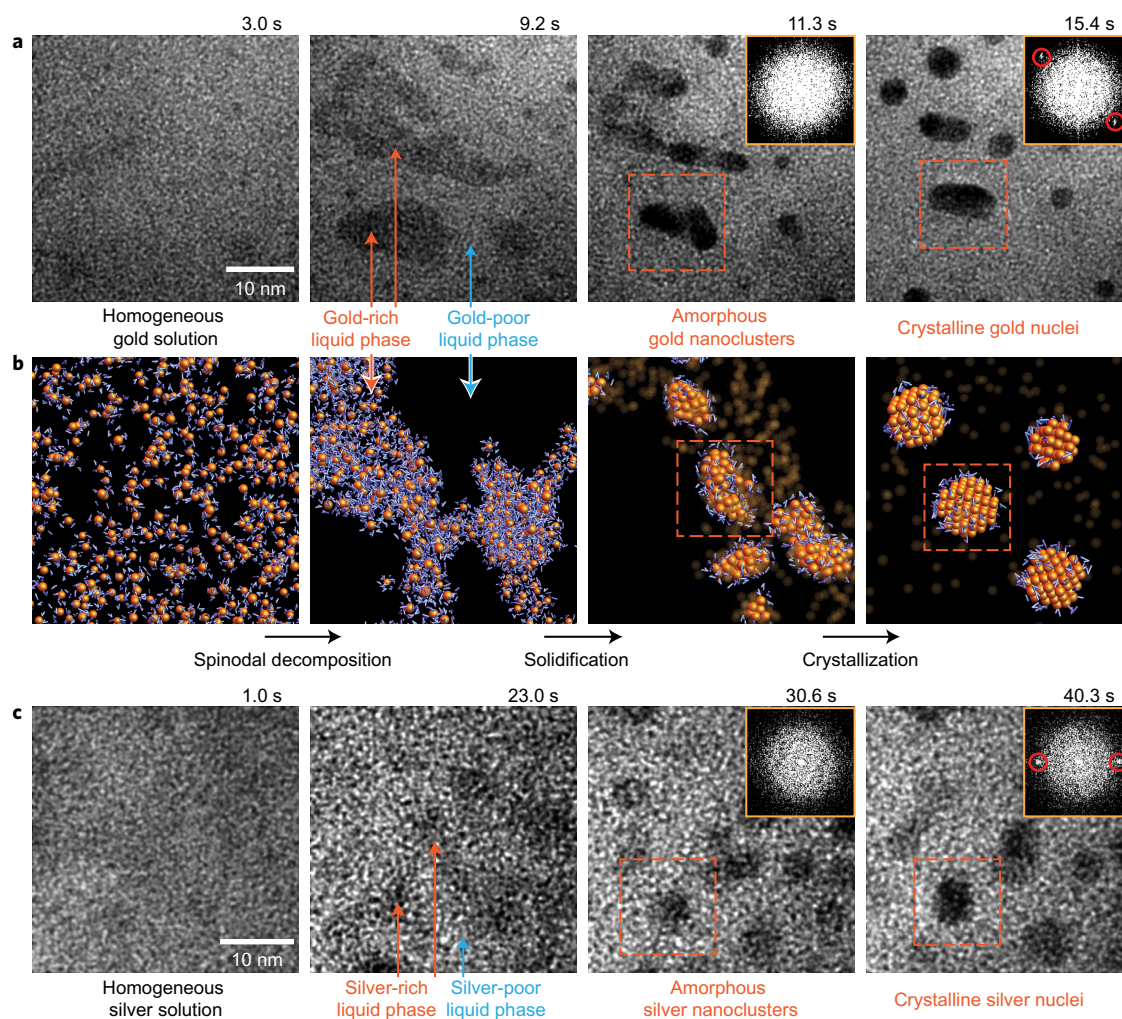


Figure 1 | Proposed three-step pathway for gold and silver nucleation in solution. a, A series of TEM images that shows the intermediate steps in nucleating gold nanocrystals from a supersaturated aqueous Au^0 solution (Supplementary Movie 1). From 3.0 to 9.2 s, the supersaturated Au^0 solution spontaneously demixes into gold-poor and gold-rich liquid phases (lighter and darker regions, respectively) via spinodal decomposition. Amorphous gold nanoclusters emerge (11.3 s) from the gold-rich phases that then crystallize (15.4 s). Insets show Fourier transforms of cropped square regions (orange) with the Au(111) fcc reciprocal lattice spacing circled in red. **b**, Schematic of the proposed steps in nucleation (gold as orange spheres, with surrounding water as blue bent lines) discussed in the text. **c**, A TEM image sequence in which silver nanocrystals nucleate from aqueous Ag^0 with the same intermediate steps as for gold in **a**. Here a supersaturated Ag^0 aqueous solution demixes into silver-poor and silver-rich liquid phases (1.0–23.0 s), and the latter develops amorphous Ag nanoclusters (30.6 s) that crystallize (40.3 s). Insets show Fourier transforms of cropped square regions (orange) with the visible Ag{111} lattice spacing circled in red.

To identify the mechanisms of gold-nanoparticle formation, we examined the initial steps of the formation of the gold-rich phase and its transition into nanoclusters of diameters between 10 and 38 Å (Fig. 2a). From mass measurements by scanning transmission electron microscopy (STEM) of amorphous nanoclusters (Supplementary Fig. 4a), we estimate that the gold concentration in the pre-nucleation gold-rich aqueous phase is ~ 4 M. Calculating backwards by redistributing the atoms in tracked amorphous nanoclusters (assumed to have the density of bulk gold) uniformly over a 30 nm thick liquid film (Supplementary Section 5), we estimate that the initial homogeneous gold concentration must have been 0.2–0.6 M (Fig. 2b) or 200–600 times more concentrated than the initial 1 mM solution (Supplementary Section 5, and motivated by Supplementary Section 7). This increase in AuCl_4^- concentration is consistent with the distribution of counterions near the positively charged SiN_x surface (Supplementary Section 7). Similar to the radiolysis-induced silver nucleation in water¹⁶, our system achieves its threshold induction dose for nucleation sooner with higher electron fluxes, and thereby also accelerates the formation of amorphous

nanoclusters (Fig. 2b). These nucleation rates are consistent with those from previous observations of gold nucleation (Supplementary Section 11A).

These amorphous nanoclusters display a range of dynamics (Supplementary Section 8) that include diffusion, rotation, coalescence and shrinking and/or growing via Ostwald ripening²⁴ or accretion²⁵. By tracking the clusters, we calculate an effective planar diffusion coefficient D_{MSD} of about 5–10 Å² s⁻¹ (Fig. 2c)²⁶ (MSD, mean square displacement), which is nine orders of magnitude smaller than the nanoparticle diffusion coefficient in bulk solution (Supplementary Sections 7 and 10). The suppressed diffusion in thin water films is consistent with previous studies, and is commonly attributed to the interaction of nanoparticles with the membrane surface and/or the few water layers adsorbed on the membrane surface^{15,26,27}. This is the reason why we are able to follow all the steps of the nucleation process at our experimental timescales of ten frames per second. From D_{MSD} we estimate an average translational blur of ~ 1.4 Å between images of a 10 Å radius gold nanocrystal separated by 100 ms,

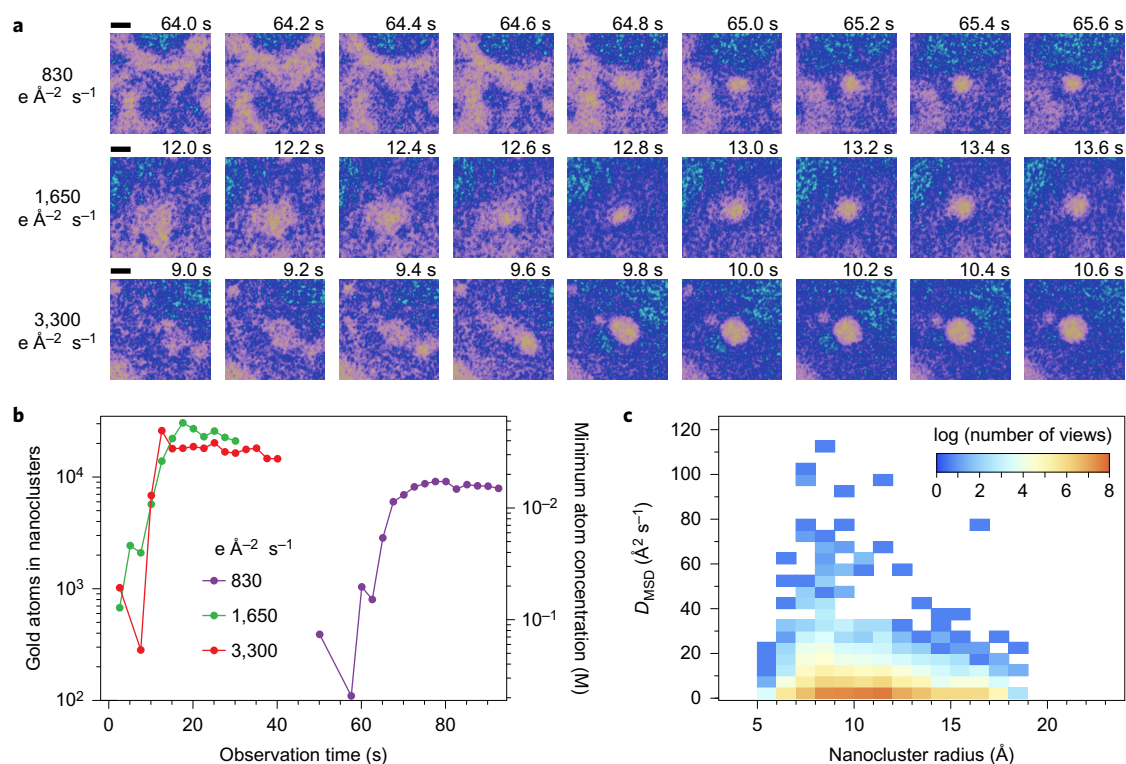


Figure 2 | Amorphous gold nanoclusters appear from gold-rich spinodal structures. **a**, High-resolution detail of three gold nanoclusters forming from spinodal structures at three TEM electron fluxes, labelled with the duration of TEM electron irradiation. Scale bars, 2 nm. The boundaries between gold-poor (dark) and gold-rich (light) regions are enhanced in this false colour image (details in Supplementary Section 8). Compact boundaries of nascent gold nanoclusters appear after 65, 12.8 and 9.8 s of observation at electron fluxes 830, 1,650 and 3,300 $\text{e} \text{Å}^{-2} \text{s}^{-1}$, respectively (Supplementary Movies 2, 3 and 1 respectively). **b**, Estimated number of gold atoms in nanoclusters assumed to be of bulk gold density when imaged with the three electron fluxes. As nanoclusters diffuse slowly, this number gives a lower bound to the initial homogeneous concentration of atomic gold dissolved in a 30 nm thick liquid film (thickness estimated in Supplementary Section 5). **c**, Histogram of nanocluster radius versus planar diffusion coefficients. This was computed from more than 15,000 consecutive pairs of TEM frames at the three electron fluxes in **b** for 74 nanoclusters that we tracked for at least five seconds each. Comparatively, the diffusion coefficient of a 1 nm radius spherical nanocluster in room-temperature bulk water is $\sim 10^{10} \text{Å}^2 \text{s}^{-1}$ (Supplementary Section 10).

which still allows us to resolve its 2.35 Å lattice spacing (examples in Fig. 3).

As our TEM and cameras have a spatial and temporal resolution more than sufficient to determine the gold nanoclusters' crystallinities, we measured a crystallinity score (Fig. 3) from a Fourier parameter around the spatial frequencies $k = 2\pi/2.35 \text{Å}^{-1}$ (elaborated in Supplementary Section 9) of $46 \times 46 \text{Å}^2$ regions centred around each nanocluster. This score is sensitive to diffraction contrast from a gold nanocrystal's face-centred-cubic (fcc) {111} lattice spacing. Of the 74 gold nanoclusters that were tracked for Fig. 3, 20 showed statistically significant crystallinity above background contrast (with 99.9% confidence) for at least 100 ms during a five-second observation window, as detailed in Supplementary Section 9. The remaining 53 nanoclusters are amorphous, or have crystallinities below our detection threshold or do not rotate their lattice planes into view for detection. The last possibility is less likely because these nanoclusters move (Fig. 2c) and rotate substantially during the five-second observation window²⁶. Notably, a meagre 0.8% of the 12,229 views of these 74 nanoclusters show significant crystallinity (observations above the line in Fig. 3). This crystalline fraction only increases to 4% for the 620 views of nanoclusters when their radii are greater than 15 Å. In later frames, the non-crystalline nanoclusters become crystalline (Fig. 1a), which suggests that an amorphous nanocluster directly precedes a crystalline nanoparticle.

The theory of spinodal decomposition explains how small density fluctuations can cause a homogeneous solution to demix into metastable high-entropy gold-poor and low-enthalpy gold-rich aqueous

phases. Two features in Figs 1a and 2a are characteristic of spinodal decomposition. First, the initial homogeneous concentration of gold in Fig. 2b is far higher than the room-temperature saturation concentration of gold in water ($\sim 10^{-12} \text{M}$ binodal²⁸). Hence, it is plausible that our gold-water binary system is deep within its spinodal region. Second, diffusion-limited spinodal structures of feature size L typically appear on timescales $\tau_{\text{sp}} \approx L^2/D_{\text{Au}}$ (ref. 29), where D_{Au} is the molecular diffusion of gold atoms ($\sim 30 \pm 6 \text{Å}^2 \text{s}^{-1}$, extrapolated from Fig. 2c using the Stokes–Einstein diffusion equation). This is consistent with the local gold-rich phases that appear within $\tau_{\text{sp}} \approx 10 \text{s}$ of observation and, indeed, have features that measure 1.6–2.0 nanometres, as shown Fig. 2.

To explain how the gold-rich aqueous phase forms and breaks down (Figs 1a and 2a), we performed *ab initio* calculations of a hydrated gold-atom pair (Fig. 4). This hydrated atom pair becomes ionized when brought closer together: the left gold atom plus two nearby water molecules form a linear cationic coordination complex, $[\text{Au}(\text{H}_2\text{O})_2]^{+1}$, whereas the right gold atom becomes an anion surrounded by a simple hydration shell. Other (square planar and linear) complexes that involve chloride and hydroxide ligands may also participate, depending on the pH (refs 23,30) (Supplementary Section 2). For nanoclusters to form inside the gold-rich aqueous phase, pairs of gold atoms within it must be partially dehydrated. In our calculations (Fig. 4), this dehydration is delayed by a 7.6 kcal mol⁻¹ ($13.0 k_{\text{B}}T$ at $T = 295 \text{K}$) energy barrier required to breakdown the linear cationic complex (close to the gold anion). Such a barrier metastabilizes a fluidic network of hydrated ionized complexes in the gold-rich phases

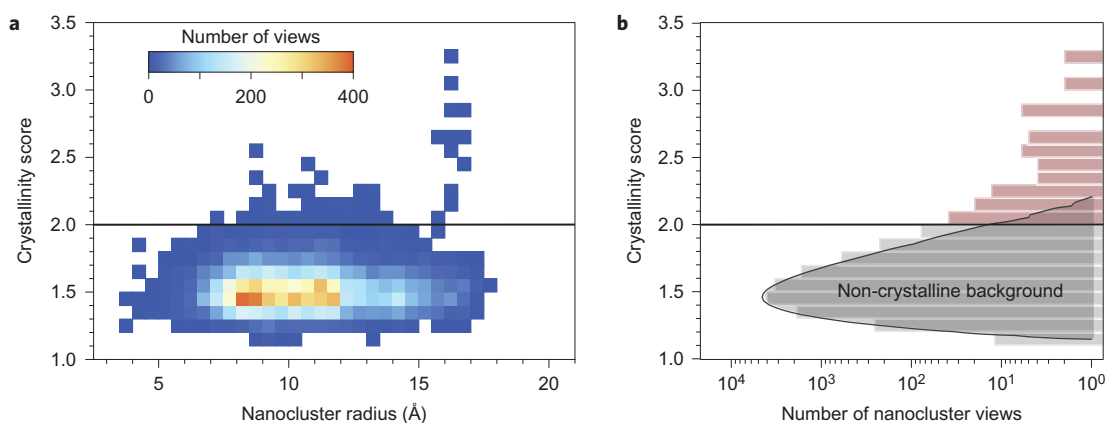


Figure 3 | Crystallinities of 74 gold nanoclusters that emerged from gold-rich phases. **a**, Crystallinity score versus cluster radii of 74 gold nanoclusters; at least 50 views on each cluster to give a total of 12,229 views. **b**, Histogram of these crystallinities, superimposed with the histogram of baseline scores for 200,000 background images that comprised only silicon nitride and water (black curve (see Supplementary Section 9)). Of the 74 nanoclusters, 20 (27%) showed statistically significant crystallinities above 2.0 (red bars) for at least 100 ms during observation windows longer than five seconds.

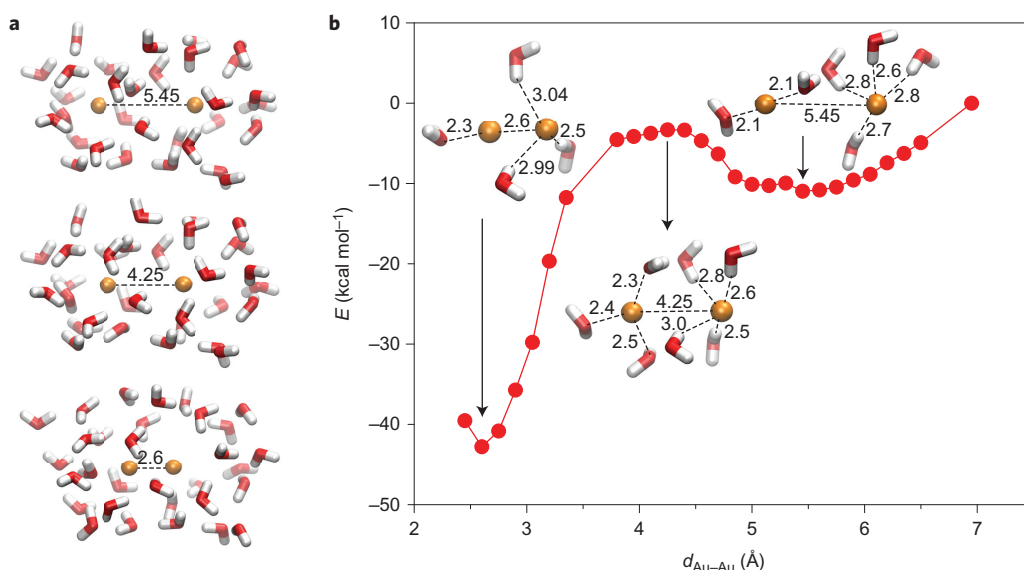


Figure 4 | Calculations of ground-state energies for a hydrated pair of gold atoms. **a**, Two gold atoms (gold spheres) were held at a separation of $d_{\text{Au-Au}}$ (Å) while the configurations of 31 surrounding water molecules (oxygen and hydrogen as red and white segments, respectively) were optimized energetically. To calculate the binding energy, we changed the distance between two gold atoms. Of 31 water molecules, 19 were completely free, whereas the oxygen atoms of the remaining 12 water molecules were fixed. **b**, The computed ground-state energy of the hydrated gold system shows two energy minima at $d_{\text{Au-Au}} = 5.45$ and 2.60 Å, with energies that differ by $31.8 \text{ kcal mol}^{-1}$. The metastable state at $d_{\text{Au-Au}} = 5.45$ Å has to overcome an energy barrier of $7.6 \text{ kcal mol}^{-1}$ by expelling intervening water molecules to access a denser Au-Au packing when $d_{\text{Au-Au}} = 2.60$ Å.

(Supplementary Sections 13 and 14) that gradually shed their waters to form amorphous nanoclusters, as illustrated in our qualitative molecular dynamics simulations (Fig. 1b and Supplementary Section 14). Most of the amorphous nanoclusters do not re-dissolve back into the gold-rich aqueous phases, as shown in Supplementary Fig. 10, which agrees with the high-energy barrier for dissolution in our calculations ($31.8 \text{ kcal mol}^{-1}$ or $54.3 k_{\text{B}}T$ at $T = 295 \text{ K}$) in Fig. 4.

Our experiment allows us to follow the evolution of intermediates present in the current nucleation. Typically, during spinodal decomposition, the surface tension between the demixed phases causes spinodal structures to coarsen and grow³¹ (also see Supplementary Fig. 21). These spinodal gold structures, shown in Fig. 1a, are unstable and condense into amorphous nanoclusters. This shrinking suggests that a second (condensed) phase transition follows the spinodal decomposition to produce amorphous nanoclusters. The amorphous organization of the $\sim 2\text{--}3 \text{ nm}$ particles is consistent with steeply decreasing melting points of gold

nanoparticles when their radii shrink below 5 nm (refs 21,32). Below this size, gold clusters that contain 20 or fewer atoms adopt a variety of non-fcc structures³³. In comparison, Li *et al.* show room-temperature platinum (which, like gold is also a noble metal) nanoparticles, become increasingly disordered when their diameters fall below 2 nm (ref. 34). These studies are compatible with how most gold clusters with diameters smaller than 3 nm that appear during multistep nucleation (Fig. 3a) are structurally amorphous. Our experimental findings show how gold-rich spinodal structures condense into amorphous nanoclusters, which then crystallize into nuclei that are large enough to be stable and support nanoparticle growth.

The spinodal gold structure is an initial step in nucleation and requires the electron beam to initiate gold-cluster formation by reducing the number of gold ions in the solution. However, we do not believe that the electron beam used in our experiments has affected the true character of multistep nucleation for the following

four reasons. First, the energy transferred by electrons heats the sample by less than 5 K (Supplementary Section 3), which rules out beam-induced melting of intermediate or final-state products. Second, evidence of spinodal decomposition was previously reported for gold nucleation even in the absence of ionizing radiation in considerably thicker liquid layers²⁰. That we resolved this transient spinodal decomposition suggests our imaging conditions did not change the nature of the intermediate steps during nucleation. Nevertheless, the multistep nucleation events reported here have yet to be observed in bulk liquid. The difference in diffusion dynamics between bulk and thin liquid, noted in Supplementary Section 10, may prevent the direct observation of the nucleation dynamics in bulk liquids with current state-of-the-art technology. Third, previous studies of radiolysis-induced nucleation of metallic salts^{23,35} did not conclude that increasing radiation doses would fundamentally alter the underlying chemistry that drives nucleation (Supplementary Section 4). This is consistent with our observations that spinodal decomposition always precedes nanocluster formation even when we quadruple the average electron flux (Fig. 2) or increase the peak flux by seven orders of magnitude using a scanning electron probe (Supplementary Section 6). Finally, the nucleation rates reported here are consistent with experiments without ionizing radiation or predicted from numerical simulations (Supplementary Section 11 and 12), which indicates that the mechanisms underlying nucleation were largely unaffected by the electron beam. Overall, we found no compelling evidence that the electron beam, aside from initiating nucleation, has fundamentally affected the observed mechanism of multistep nucleation.

Conclusions

Our observations clearly show that gold nanocrystals can nucleate from a supersaturated aqueous solution via a three-step mechanism: spinodal decomposition, solidification and crystallization. The amorphous nanocluster is a direct precursor for the crystalline nucleus in solution. We anticipate that this sequence could be common in crystallization. If so, then the amorphous nanocluster would be an intermediate common to the formation of both crystalline and amorphous solids from solution. More generally, this ability to observe pathways in crystal nucleation will impact research on catalysis, nanoparticle synthesis and structural biology. Our findings show that multistep nucleation pathways are feasible, quantifiable and will help to develop better and broadly applicable nucleation models.

Methods

We used *in situ* TEM to follow the nucleation dynamics of gold from an aqueous 1 mM HAuCl₄ solution sealed in a microfabricated liquid cell^{15,36,37} that comprised two ultrathin (~14 nm) SiN_x membranes separated by ~200 nm spacers (Supplementary Section 1) at a frame rate of 10 Hz. When irradiated by electrons, the bulk of the aqueous solution recedes, leaving a ~30 nm thick aqueous film³⁸ (details in Supplementary Sections 2–5) in which the gold ions are reduced *in situ* by the electron beam and eventually form gold nanoparticles. This approach enables us to track the nucleation of these gold nanoparticles with insignificant thermal perturbation (Supplementary Section 3) and eliminating chemical reducing agents.

Two different TEMs were used for *in situ* imaging, JEOL 2010FEG for TEM imaging and FEI Titan for STEM imaging, both with 200 kV electrons at doses that ranged from 800 to 8,000 e⁻ Å⁻² s⁻¹. We recorded movies at a frame rate of 10 Hz and at a magnification of ×250,000 to ×400,000 using an Orius SC200 CCD (charge-coupled device) camera (Gatan).

Received 8 May 2016; accepted 18 August 2016;
published online 3 October 2016

References

- Sear, R. P. The non-classical nucleation of crystals: microscopic mechanisms and applications to molecular crystals, ice and calcium carbonate. *Int. Mater. Rev.* **57**, 328–356 (2012).
- De Yoreo, J. J. & Vekilov, P. G. in *Biomaterialization* (eds Dove, P., De Yoreo, J. & Weiner, S.) 57–93 (Mineralogical Society of America, 2003).
- Vekilov, P. G. Dense liquid precursor for the nucleation of ordered solid phases from solution. *Cryst. Growth Des.* **4**, 671–685 (2004).
- Kalikmanov, V. I. *Nucleation Theory* (Lecture Notes in Physics Vol. 860, Springer, 2013).
- De Yoreo, J. J. *et al.* Crystallization by particle attachment in synthetic, biogenic, and geologic environments. *Science* **349**, aaa6760 (2015).
- Hill, P. G. Condensation of water vapour during supersonic expansion in nozzles. *J. Fluid Mech.* **25**, 593–620 (1966).
- Vekilov, P. G. The two-step mechanism of nucleation of crystals in solution. *Nanoscale* **2**, 2346–2357 (2010).
- Sanz, E. *et al.* Homogeneous ice nucleation at moderate supercooling from molecular simulation. *J. Am. Chem. Soc.* **135**, 15008–15017 (2013).
- De Yoreo, J. Crystal nucleation: more than one pathway. *Nat. Mater.* **12**, 284–285 (2013).
- Erdemir, D., Lee, A. Y. & Myerson, A. S. Nucleation of crystals from solution: classical and two-step models. *Acc. Chem. Res.* **42**, 621–629 (2009).
- Cahn, J. W. & Hilliard, J. E. Free energy of a nonuniform system. III. Nucleation in a two-component incompressible fluid. *J. Chem. Phys.* **31**, 688–699 (1959).
- Wallace, A. F. *et al.* Microscopic evidence for liquid–liquid separation in supersaturated CaCO₃ solutions. *Science* **341**, 885–889 (2013).
- Nielsen, M. H., Aloni, S. & De Yoreo, J. J. *In situ* TEM imaging of CaCO₃ nucleation reveals coexistence of direct and indirect pathways. *Science* **345**, 1158–1162 (2014).
- Vekilov, P. G. Phase diagrams and kinetics of phase transitions in protein solutions. *J. Phys. Condens. Matter* **24**, 193101 (2012).
- Zheng, H. *et al.* Observation of single colloidal platinum nanocrystal growth trajectories. *Science* **324**, 1309–1312 (2009).
- Woehl, T. J., Evans, J. E., Arslan, I., Ristenpart, W. D. & Browning, N. D. Direct *in situ* determination of the mechanisms controlling nanoparticle nucleation and growth. *ACS Nano* **6**, 8599–8610 (2012).
- Patterson, J. P. *et al.* Observing the growth of metal–organic frameworks by *in situ* liquid cell transmission electron microscopy. *J. Am. Chem. Soc.* **137**, 7322–7328 (2015).
- Tromp, R. M. & Ross, F. M. Advances in *in situ* ultra-high vacuum electron microscopy growth of SiGe on Si. *Annu. Rev. Mater. Sci.* **30**, 431–449 (2000).
- Privman, V., Goia, D. V., Park, J. & Matijevic, E. Mechanism of formation of monodispersed colloids by aggregation of nanosize precursors. *J. Colloid Interface Sci.* **213**, 36–45 (1999).
- Mikhlin, Y. *et al.* Submicrometer intermediates in the citrate synthesis of gold nanoparticles: new insights into the nucleation and crystal growth mechanisms. *J. Colloid Interface Sci.* **362**, 330–336 (2011).
- Sambles, J. R. An electron microscope study of evaporating gold particles: the Kelvin equation for liquid gold and the lowering of the melting point of solid gold particles. *Proc. R. Soc. Lond. A.* **324**, 339–351 (1971).
- Chushak, Y. G. & Bartell, L. S. Melting and freezing of gold nanoclusters. *J. Phys. Chem. B* **105**, 11605–11614 (2001).
- Gachard, E. *et al.* Radiation-induced and chemical formation of gold clusters. *New J. Chem.* **22**, 1257–1265 (1998).
- Xin, H. L. & Zheng, H. *In situ* observation of oscillatory growth of bismuth nanoparticles. *Nano Lett.* **12**, 1470–1474 (2012).
- Aabdin, Z. *et al.* Bonding pathways of gold nanocrystals in solution. *Nano Lett.* **14**, 6639–6643 (2014).
- Lu, J., Aabdin, Z., Loh, N. D., Bhattacharya, D. & Mirsaidov, U. Nanoparticle dynamics in a nanodroplet. *Nano Lett.* **14**, 2111–2115 (2014).
- Park, J. *et al.* 3D structure of individual nanocrystals in solution by electron microscopy. *Science* **349**, 290–295 (2015).
- Seidell, A. & Linke, W. F. *Solubilities of Inorganic and Metal–Organic Compounds* (Van Nostrand, 1958).
- Laughlin, D. E. & Soffa, W. Spinodal structures. *ASM Handbook* **9**, 652–654 (1985).
- Dey, G. R., El Omar, A. K., Jacob, J. A., Mostafavi, M. & Belloni, J. Mechanism of trivalent gold reduction and reactivity of transient divalent and monovalent gold ions studied by gamma and pulse radiolysis. *J. Phys. Chem. A* **115**, 383–391 (2011).
- Rappl, T. J. & Balsara, N. P. Does coarsening begin during the initial stages of spinodal decomposition? *J. Chem. Phys.* **122**, 22–25 (2005).
- Guenther, G. & Guillon, O. Models of size-dependent nanoparticle melting tested on gold. *J. Mater. Sci.* **49**, 7915–7932 (2014).
- Gruene, P. *et al.* Structures of neutral Au₇, Au₁₉, and Au₂₀ clusters in the gas phase. *Science* **321**, 674–676 (2008).
- Li, L. *et al.* Noncrystalline-to-crystalline transformations in Pt nanoparticles. *J. Am. Chem. Soc.* **135**, 13062–13072 (2013).
- Belloni, J. Nucleation, growth and properties of nanoclusters studied by radiation chemistry application to catalysis. *Catal. Today* **113**, 141–156 (2006).
- Williamson, M. J., Tromp, R. M., Vereecken, P. M., Hull, R. & Ross, F. M. Dynamic microscopy of nanoscale cluster growth at the solid–liquid interface. *Nat. Mater.* **2**, 532–536 (2003).

37. Ross, F. M. Opportunities and challenges in liquid cell electron microscopy. *Science* **350**, aaa9886 (2015).
38. Mirsaidov, U. M., Zheng, H., Bhattacharya, D., Casana, Y. & Matsudaira, P. Direct observation of stick-slip movements of water nanodroplets induced by an electron beam. *Proc. Natl Acad. Sci. USA* **109**, 7187–7190 (2012).

Acknowledgements

This work was supported by the Singapore National Research Foundation's Competitive Research Program funding (NRF-CRP9-2011-04) and the Young Investigator Award (NUSYA-FY14-P17) from the National University of Singapore. C.A.N. and M.B. acknowledge support from grant No. NRF-CRP8-2011-07, U.M. and P.M. acknowledges support from the Microbiology Institute (Singapore) and the Centre for Bioimaging Sciences. N.D.L. thanks the support of the Lee Kuan Yew Endowment Fund, and National University of Singapore internal grant No. 154-000-606-112. The work of P.K. was supported by the National Science Foundation Division of Materials Research Grant No. 1309765 and by the American Chemical Society Petroleum Research Funding Grant No. 53062-ND6.

Author contributions

U.M. and P.M. conceived the study. U.M. designed the *in situ* experiments, which he performed together with M.B. and S.F.T.; N.D.L. designed and implemented the image processing and statistical analysis on the TEM images, with help from J.Z. and input from U.M., P.M., C.A.N. and M.B.; N.D.L. did and, with U.M. and M.B., wrote up the analyses in the Supplementary Information on CNT, spinodal decomposition and the effects of the electron beam. S.S. and P.K. carried out the hybrid molecular dynamics calculations. N.D.L., C.A.N., P.K., P.M. and U.M. wrote the manuscript from discussions that arose from all authors.

Additional information

Supplementary information is available in the [online version of the paper](#). Reprints and permissions information is available online at www.nature.com/reprints. Correspondence and requests for materials should be addressed to C.A.N., P.K. and U.M.

Competing financial interests

The authors declare no competing financial interests.